

AFM and Acoustics: Fast, Quantitative Nanomechanical Mapping

Bryan D. Huey

Institute of Materials Science, University of Connecticut, Storrs, Connecticut
06269-3136; email: bhuey@ims.uconn.edu

Annu. Rev. Mater. Res. 2007. 37:351–85

The *Annual Review of Materials Research* is online at
<http://matsci.annualreviews.org>

This article's doi:
10.1146/annurev.matsci.37.052506.084331

Copyright © 2007 by Annual Reviews.
All rights reserved

1531-7331/07/0804-0351\$20.00

Key Words

nanomechanics, ultrasonic, high speed, contact mechanics, SPM

Abstract

Combining atomic force microscopy and ultrasonic methods allows near-field detection of acoustic signals and thereby otherwise inaccessible nanoscale mechanical characterization. The two predominant variations, ultrasonic force microscopy and atomic force acoustic microscopy, are reviewed in detail. Applications of each to ceramics, polymers, metals, biological materials, and even subsurface structures are discussed, with a particular emphasis on image contrast mechanisms, data analysis, and experimental challenges. Finally, recent advances of these concepts into high-speed surface property mapping are presented, demonstrating 100-fold enhancements in full-frame imaging speeds.

SPM: scanning probe microscopy

AFM: atomic force microscopy

UFM: ultrasonic force microscopy

AFAM: atomic force acoustic microscopy

INTRODUCTION

Since the advent of scanning probe microscopy (SPM) in 1981, a multitude of new SPM variations have been developed to measure a broad range of properties under widely varying conditions (1). One important class of such SPM-based measurements couples SPM and acoustic methods. Standard ultrasonic techniques, for example, scanning acoustic microscopy (2), are widely applied in nondestructive testing because of their capabilities for quantitative mechanical measurements and to identify surface and even buried structures. However, the spatial resolution is limited by Abbe's principle to features roughly equivalent to the ultrasonic wavelength. For most solids at typical ultrasonic frequencies (1 GHz down to 1 MHz), the theoretical lower limit on resolution is thus on the order of micrometers to millimeters, respectively (determined on the basis of the velocity of sound propagation in the sample divided by the ultrasonic frequency). Coupling SAM with SPM, however, provides the potential for far-better spatial resolution by detecting acoustic signals in the near field, analogous to the enhancement in spatial resolution achieved with near-field-optical-microscopy methods over traditional far-field optical microscopy. The resulting image contrast is indicative of the mechanical properties of the surface at the nanoscale and is usually acquired simultaneously as standard topographic atomic force microscopy (AFM) imaging, as exemplified by the images in **Figure 1**. Many variations of such acoustic-SPM combinations have been conceived by the SPM and acoustics communities, but two methods in particular have received the most attention and are thus the focus of this review. These are ultrasonic force microscopy (UFM), originally developed by Kolosov & Yamanaka (3) and Yamanaka et al. (4), and atomic force acoustic microscopy (AFAM), developed by Rabe & Arnold (5). Novel recent extensions of these concepts to high-speed scanning by Huey et al. are also discussed.

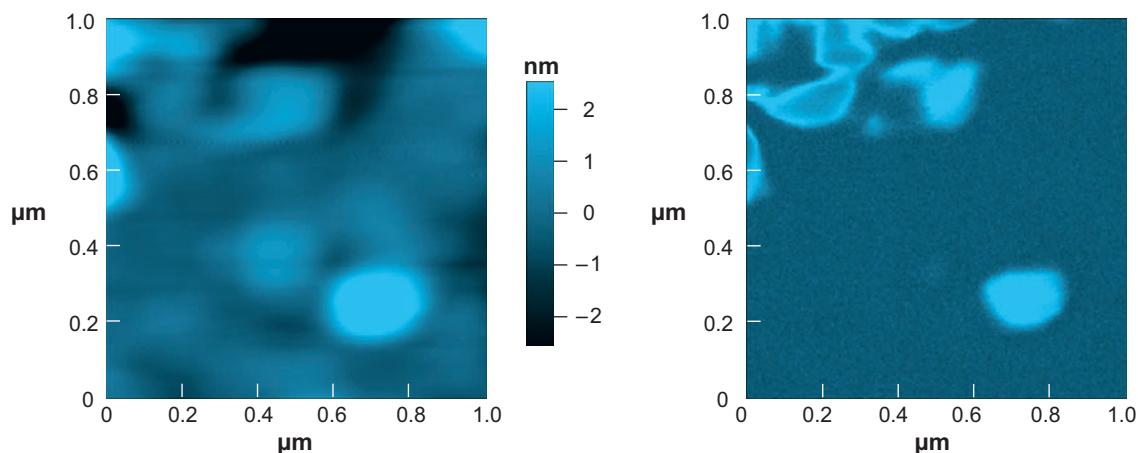


Figure 1

AFM (*left*) and AFAM (*right*) images of Au nanoislands on Si.

BACKGROUND

Before coupled AFM and ultrasonic methods are addressed in detail, a review of contact mechanics and force sensing with AFM tips and cantilevers is crucial, as all ultrasonic-AFM methods developed thus far incorporate tip-sample contact.

Contact Mechanics

Ultrasonic applications of AFM are rooted in the contact mechanics between the AFM tip and the sample surface. Such interactions have been studied for more than a century, and the dominant equation upon which most modern AFM mechanical analyses are based stems from work published by Hertz in the 1890s (Equation 1). The repulsive Hertzian force (F_{Hertz}) experienced by a sphere indented into a surface is simply proportional to the separation (s , in this case indentation), a radius term (R), and a constant related to the elastic properties of the tip and sample (K) (6). This presumes purely elastic loading, tip and sample materials that are not viscoelastic, and no adhesion between the tip and sample.

$$F_{Hertz} = K\sqrt{R}s^{2/3}. \quad 1.$$

R is actually the reduced radius of curvature, which incorporates the radii of the AFM tip and sample (Equation 2). K is the reduced modulus, depending on the elastic moduli (E) and Poisson's ratios (ν) of the tip and sample (Equation 3). Although rigorous only for bulk, isotropic materials, anisotropic or surface properties are often simply substituted. Furthermore, although the spherical approximation of the tip shape is generally appropriate for AFM measurements, in some circumstances a flat punch geometry is applicable owing to tip blunting. In this case, the Hertzian force is linear with the indentation.

$$\frac{1}{R} = \frac{1}{r_{tip}} + \frac{1}{r_{sample}}, \quad 2.$$

$$\frac{1}{K} = \frac{3}{4} \left[\frac{(1 - \nu_{tip})^2}{E_{tip}} + \frac{(1 - \nu_{sample})^2}{E_{sample}} \right]. \quad 3.$$

In reality, adhesion often occurs between two surfaces such that upon contact an attractive force is experienced. This is generally addressed with the more sophisticated DMT or JKRS models, primarily applicable to cases of small or large surface energies (ω), respectively. In the JKRS model (7, 8), the possibility of indenting and retracting hysteresis is also incorporated to account for the observed behavior whereby after contact the tip remains attached to the surface even for positive separations. More quantitatively, but requiring numerical instead of analytical analyses, the Maugis method describes a great range of experimental conditions (9). Conveniently, the Maugis model incorporates both DMT and JKRS mechanics, using one primary term (λ), defined in Equation 4. Lambda itself depends on the reduced radius, adhesion energy, reduced modulus, and equilibrium interatomic separation (ξ_0). For vanishingly small λ ($\ll 1$), Maugis mechanics mimic the DMT model, appropriate for small radius, small surface energy, and high stiffness contacts. For the opposite

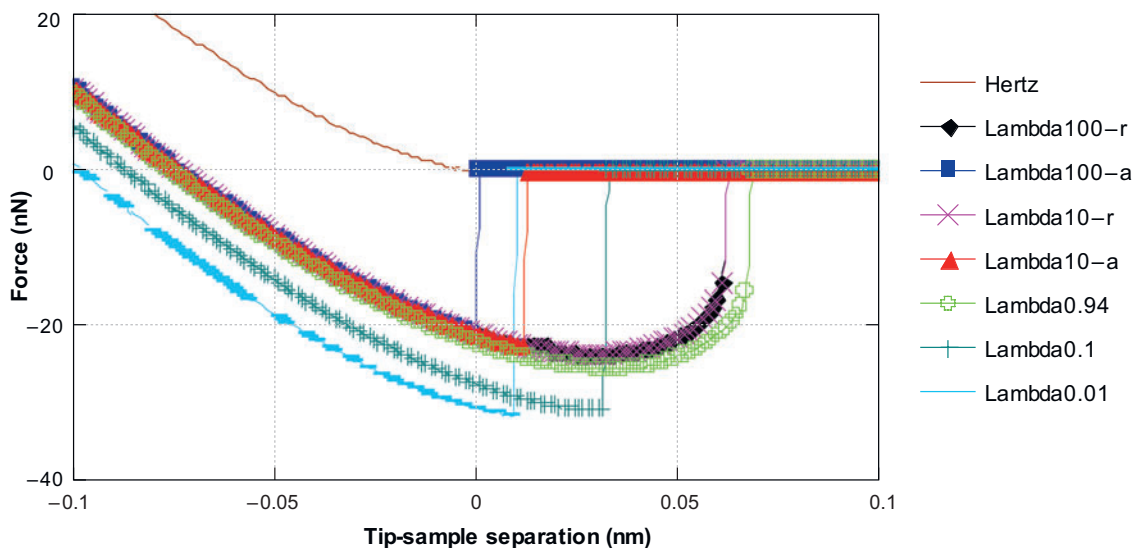


Figure 2

Force-versus-tip-sample separation for a Hertz model as well as for various Maugis lambda parameters.

experimental conditions, particularly those incorporating hysteretic approaches and retractions, large λ values (>10) are employed, mimicking the JKRS description. Regardless of the model, however, the behavior upon indentation follows the familiar Hertzian trend; that is, the force experienced by the tip and sample is proportional to the indentation to the $3/2$ power.

$$\lambda = \frac{2.06}{\xi_0} \left(\frac{R\omega^2}{\pi K^2} \right)^{1/3} \quad 4.$$

Figure 2 presents the force experienced by a spherical tip obeying Maugis mechanics with several representative λ parameters; this force is plotted as a function of tip-sample separation. The origin is fixed as the point of contact, assuming rigid bodies. Positive and negative forces are repulsive and attractive, respectively. For a probe initially indented into a surface (negative separation), the initially repulsive forces are relaxed upon tip withdrawal, transitioning to attractive forces in the event of surface adhesion. The surface and tip may even bulge toward each other so that contact is maintained even though the separation is positive to an extent that depends on experimental conditions. In general, the pull-off separation increases and the pull-off force diminishes as λ increases until approximately 0.94, after which they remain constant. Physically, upon retraction the connecting neck between the tip and sample elongates until the tip abruptly pulls off of the surface and the surface relaxes. This loss of contact occurs once the separation increases sufficiently that the force gradient (dF/ds) approaches infinity, a constraint known as fixed grips. This is assumed to occur

instantaneously, after which the probe experiences no force for further separations. The effects of any long-range interactions—including van der Waals, electromagnetic, or capillary forces (resulting from the presence of a water layer between the tip and sample)—can also be superimposed, but these are ignored here for relative simplicity.

When the surface (+ to – separation) is reapproached, a sudden attractive jump to contact may occur in the event of surface adhesion. Once again, this may occur for positive separations if the tip and sample surfaces bulge toward each other. For experimental conditions such that $\lambda < 0.94$, contact is reestablished at the same separation as it was lost (there is no adhesion hysteresis). For larger λ values, lesser separations and higher attractive forces are predicted for approaching as opposed to retracting tips (**Figure 2**) [the exact separation for reattachment is discussed extensively elsewhere (9)]. These details are crucial to an understanding of ultrasonic-AFM interactions because the shape of the $F(s)$ curve, indeed λ itself, varies depending on the tip and sample mechanical properties, energy of adhesion, and reduced radii of curvature. Furthermore, for $\lambda > 0.94$, the act of approaching and retracting a tip and sample is inherently hysteretic owing to different separations for making and losing contact. Each of these points influences ultrasonic and AFM measurements, as discussed below.

Cantilever Force Detection

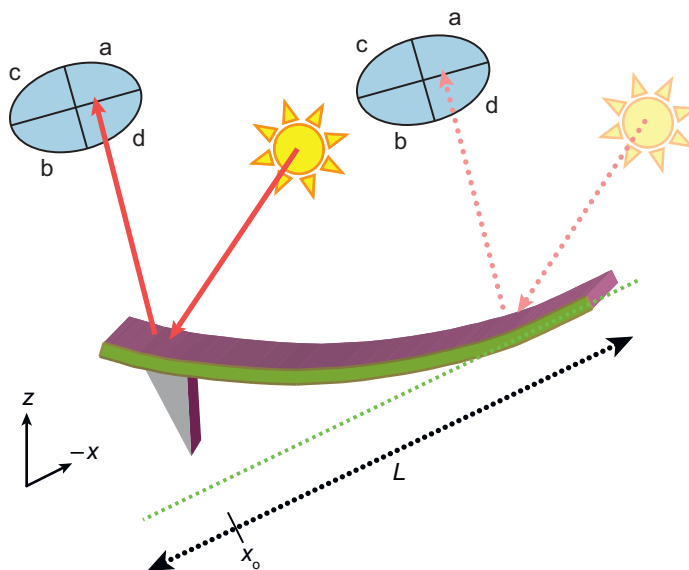
Forces in AFM are usually transduced by optically detecting any deflection of a cantilever near the end of which the tip is attached. This measured deflection is reasonably assumed to behave as an elastic spring and obey Hooke's law (Equation 5), incorporating the lever spring constant (k_c). In practice, however, the detected deflection is generally measured by reflecting a focused laser or LED beam onto a photodiode (**Figure 3**). The equation defining the actual force at the tip (Equation 6) then accounts for the focal point (detector position) along the lever (x), the lever length (L), and the tip position along the lever (x_0 , usually $>90\%$ L). This model is appropriate for purely local investigations in which the lever only experiences loads at the tip instead of distributed loads. When long-range loads are applied, though, several corrections should rigorously be included (10). The most important point here is that the actual force applied at the tip can vary from one measurement to the next, depending on the AFM laser alignment (x), which will influence all quantitative AFM and ultrasonic measurements. Calibration procedures are therefore important whenever a cantilever, or even the detecting laser, is aligned.

$$F_{tip} = F_{measured} = k_c z_{deflection} = k_c (d' - d_{sp}). \quad 5.$$

$$F_{tip} = k_c z \left[\frac{2L^3}{x^2(x - 3x_0)} \right]. \quad 6.$$

Figure 3

Sketch of a typical cantilever deflection detection scheme. L denotes the lever length, x_0 denotes the distance from tip from base, and a–d signify the independent quadrants of the segmented photodetector.



METHODS

This section discusses a few general details, followed by specifics about actually making and interpreting measurements based on UFM and AFAM.

General

Coupling ultrasonic and AFM methods evidently requires ultrasonic excitations of the sample and/or tip. This is typically achieved by launching longitudinal waves through the thickness of a sample by actuating an attached piezo-transducer. This attachment is generally achieved by direct deposition onto the actuator surface or by applying various glues, gels, or even honey. Through the application of a sinusoidal bias to the actuator, the converse piezoelectric effect causes the actuator to expand and contract, creating traveling waves that cause the sample surface to vibrate with an Ångstrom-scale amplitude. Alternatively, the tip may be excited with an actuator at its base and, owing to its geometry, will act as a waveguide. Broadband or resonant actuators can be employed, although other means of actuation, including electrostatic attraction, direct sample piezoactuation, and pulsed laser-induced thermal excitation, have also been employed.

The hardware necessary for ultrasonic and AFM measurements includes MHz-frequency-bandwidth signal generators, amplifiers, filters, attenuators, mixers, and oscilloscopes. Lock-in amplifiers are also crucial to detecting the subnanometer-scale signals that must be analyzed, especially as the data are superimposed on comparatively noisy scanning cantilever deflection signals. Indeed, ultrasonic AFM methods typically require the detection of periodic ultrasonic signals several orders of

magnitude smaller than the aperiodic cantilever deflection that results from simultaneous AFM scanning. Nevertheless, ultrasonic methods employing a variety of commercial cantilevers have been carried out, and measurements have been performed on numerous custom and commercial AFM systems as long as the lever detection signal can be accessed with an appropriate bandwidth. Increasingly available are newer AFM models that incorporate extensive signal access to input/output channels and ever higher detector bandwidths, which usually determines the upper frequency limit for ultrasonic applications in AFM. Cabling should all be coaxial.

Ultrasonic Force Microscopy

UFM relies upon three primary principles: (a) dynamic stiffening of an AFM cantilever for super-resonant periodic excitations, (b) a corresponding periodic indentation of an AFM tip contacting a vibrating sample surface, and (c) a detectable average force experienced by the tip per excitation period that depends sensitively on the mechanics of the tip-sample contact and thereby on the sample properties. This section describes this mechanism and its applications in detail.

Ultrasonic indentations. To understand a UFM measurement, it is instructive to consider a typical force-separation curve (**Figure 4**). Initially, the tip is not scanned and simply contacts a surface with a user-defined repulsive setpoint force (F_{sp}) and thus a fixed setpoint indentation (s_{sp}) (point a in **Figure 4**). The ultrasonic actuator to which the sample is attached is then activated with a sinusoidal excitation, causing the sample surface to oscillate with an amplitude of u_a at a frequency of ω . If the drive frequency is beyond the lever resonance, however, the lever response is inertially

JOA: jump-off amplitude (JOA_i and JOA_d denote increasing or decreasing ultrasonic amplitudes, respectively)

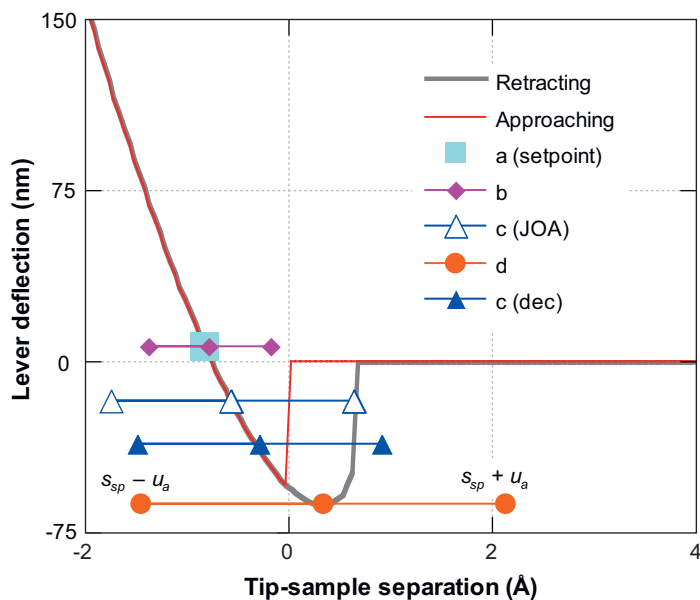


Figure 4
AFM cantilever deflection versus tip-sample separation during UFM with varying applied ultrasonic amplitudes ($a = 0 \text{ \AA}$, $b = 0.6 \text{ \AA}$, $c = 1.2 \text{ \AA} = \text{JOA}_i$, $d = 1.8 \text{ \AA}$).

limited, effectively increasing the dynamic lever stiffness. Because the tip cannot follow the surface vibration, the obvious alternative is that the probe instead periodically indents the sample. Of course, a smooth transition between these behaviors is likely, but a simplifying assumption is generally made: The entire amplitude for an ultrasonic actuation of a contacting probe is transferred to the periodic indentation. In other words, the tip remains stationary on the timescale of the ultrasonic excitation such that the surface periodically indents itself on the fixed tip.

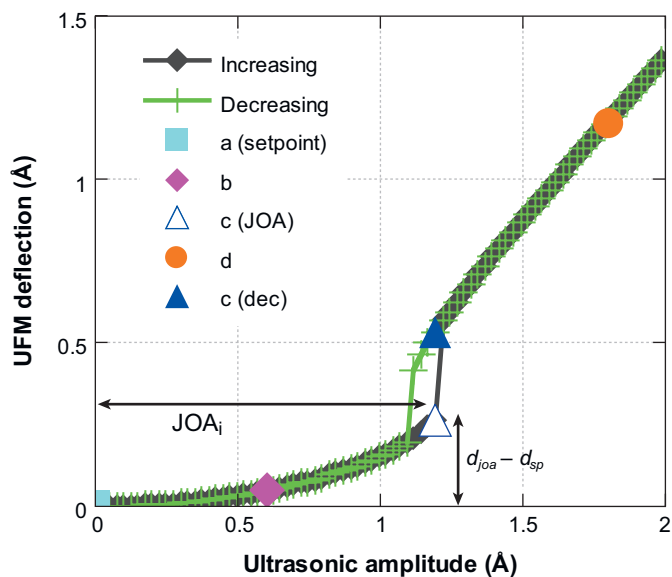
Because the tip is stationary but the surface is oscillating, the instantaneous force experienced by the probe also oscillates, essentially tracing the force-separation curve between two extremes defined by the ultrasonic amplitude, $s_{sp} - u_a$ and $s_{sp} + u_a$ (sketched in **Figure 4**). As the lever cannot deflect in response at such high speeds, however, it is more appropriate to consider the average force experienced by the AFM tip during each periodic vibration. This is determined by integrating the instantaneous force over the period and normalizing to the period time (Equation 7).

$$\bar{F} = \left(\frac{\omega}{2\pi} \right) \int_0^{2\pi/\omega} F(s_{sp} - u_a \cos(\omega t)) dt. \quad 7.$$

Of course, the average forces of UFM are transduced to deflection by the AFM cantilever (Equation 5), yielding UFM force spectra as shown in **Figure 5**. The astute observer will recognize that these deflection signals imply that the tip displaces from its initial setpoint deflection (d_{sp}) for increasing excitation amplitudes, causing the indentation itself to shift as well. This has the effect of shifting the center point of the ultrasonic vibration (\bar{d}_a) toward the origin and hence also changes the range of forces accessed during the ultrasonic actuation. These subtleties are depicted in **Figures 4** and **5**, which highlight four distinct ultrasonic amplitudes (0, 0.6, 1.2, and 1.8 Å). In this manner the tip effectively accelerates out of contact as the amplitude is increased.

Figure 5

UFM spectra of cantilever deflection versus ultrasonic excitation, highlighting the same ultrasonic amplitudes as in **Figure 4** ($a = 0$ Å, $b = 0.6$ Å, $c = 1.2$ Å = JOA_i , $d = 1.8$ Å).



Incorporating this detail into Equations 5 and 7 finally provides the most accurate description of the average deflection ($\bar{d}_a - d_{sp}$) detected during UFM (Equation 8).

$$\bar{d}_a - d_{sp} = \frac{\bar{F}}{k_c} = \frac{1}{k_c} \left[\left(\frac{\omega}{2\pi} \right) \int_0^{2\pi/\omega} F(s_{sp} + (\bar{d}_a - d_{sp}) - u_a \cos(\omega t)) dt - F_{sp} \right]. \quad 8.$$

For small amplitudes and large repulsive setpoint forces (indentations), the average force is nearly identical to the setpoint value because contact forces generally vary with indentation to the $3/2$ power. As the amplitude increases, the curvature of the force-versus-indentation response causes the average force to increase subtly. More significant, however, is when the ultrasonic amplitude is increased sufficiently that the tip and sample briefly lose contact once per period. The abrupt repulsive force variation, usually from an attractive load to zero, now substantially increases the average force experienced by the tip during the entire ultrasonic period. This is the practical basis for the contrast mechanism in UFM because the nonlinear change in the average force (deflection) depends sensitively on the shape of the F - s curve (most strongly on when the tip and sample begin to lose contact) and hence on local sample properties.

A problem arises, however, because UFM is performed during contact AFM with the standard force feedback engaged. The AFM hardware and software therefore interpret the increase in force due to ultrasonic actuation as if the tip had encountered a protrusion. Correspondingly, the tip would be pulled away from the surface to restore the initial setpoint force. Fortunately, if the ultrasonic amplitude is modulated at a frequency too fast for the AFM system to correct, but slow enough that enough periods at any given amplitude are applied for reasonable detection, then the UFM signal can be monitored, and the AFM can detect and track topography as usual. **Figure 6**

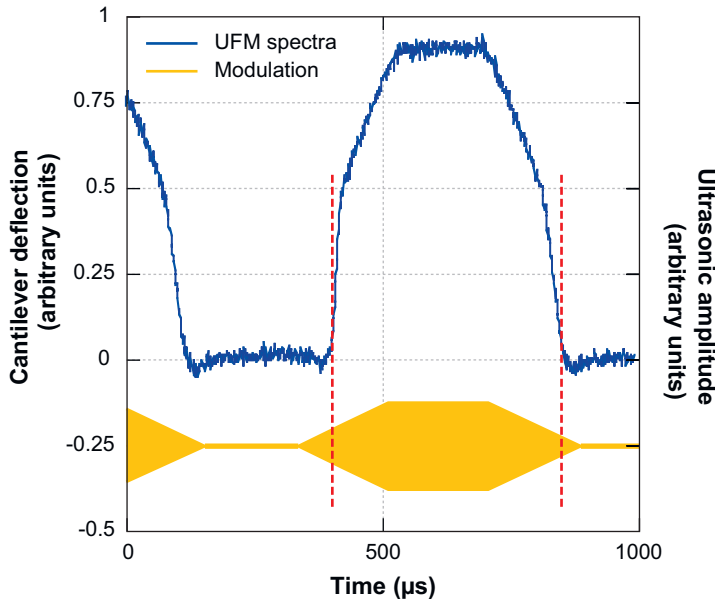


Figure 6
Typical UFM modulation signal and corresponding measured cantilever response.

presents a typical modulation waveform (base), with a measured UFM response (top). As predicted, the deflection is at its setpoint value when no ultrasonic actuation is applied, hardly changes as the ultrasonic actuation begins to increase, jumps abruptly once the jump-off amplitude (JOA) is reached, increases linearly for still-greater ultrasonic driving amplitudes, reaches a plateau for a fixed driving amplitude, decreases linearly for decreasing driving amplitudes, and finally returns abruptly to the baseline setpoint value. UFM measurements are typically performed at the same time as topographic scanning, using carrier waves in the MHz regime and modulation frequencies of a few kHz. The primary trick of UFM thus involves using the normal AFM feedback loop for standard topographic imaging while simultaneously defeating this same AFM feedback loop to excite and detect ultrasonic indentations.

Differential UFM. The characteristic ultrasonic amplitude at which the modulated UFM deflection signal increases abruptly is known as the increasing jump-off amplitude (JOA_i). Because this corresponds to when the initially indented tip and sample begin to lose contact during ultrasonic oscillations, a very simple measurement of contact stiffness is now readily apparent. That is, the initial tip indentation is merely the sum of the JOA_i plus the lever deflection just before the jump-off point ($\bar{d}_{JOA} + d_{sp}$). This initial indentation is otherwise impossible to know in AFM, and with it the slope of the measured force versus the measured indentation can be uniquely determined. Differential measurements are usually recorded at multiple setpoint forces (11, 12), giving the contact stiffness (*S*) according to Equation 9. Several such so-called differential UFM studies have been reported, although the complete solution incorporating the last two terms in the denominator of Equation 9 has not been implemented thus far.

$$S = \frac{\Delta F_{sp}}{\Delta \bar{d}_{JOA} + \Delta \bar{d}_{JOA} + \Delta d_{sp}} \quad 9.$$

UFM spectra analysis. In fact, the JOA is a sensitive function of more than just the initial AFM setpoint indentation. To demonstrate this, calculations were performed following Maugis mechanics to predict the UFM response for a reasonable range of several typical experimental parameters. The parameters included the reduced modulus (equivalently the elastic properties of the sample for a fixed tip type), adhesion energy, reduced radius, AFM setpoint force, and AFM cantilever spring constant. With so many dimensions to consider, five distinct series of calculations were performed by modifying the variables shown in **Table 1**, always maintaining default values for all other parameters as follows (also in bold in **Table 1**): reduced modulus (128 GPa), adhesion energy (0.1 J m⁻²), reduced radius (50 nm), setpoint force (2 nN), and cantilever spring constant (0.4 nN nm⁻¹). **Figure 7** presents the Maugis lambda parameter for each of these individual calculations, grouped by the property being considered. As anticipated on the basis of Equation 4, lambda is sensitive to each variable except for the spring constant and setpoint force.

After the application of each of these experimental conditions to the complete UFM response equation (Equation 8), the theoretical sensitivity of JOA_i is finally presented. **Figure 8** displays the results as a function of the experimental

Table 1 Experimental parameters individually considered^a

Reduced modulus (GPa) ^b	Adhesion energy (J m ⁻²)	Reduced radius (nm)	AFM setpoint force (nN)	Cantilever spring constant (nN nm ⁻¹)
3.9706	0.01	5	0.1	0.05
17	0.072	10	1	0.26
60	0.1	25	2	0.4
80	0.72	50	5	1.6
108.0735	1	75	10	2.7
127.774	7.2	100	20	3.2
135	10	150	50	20
200	72	200	100	100

^aNominal values are in bold.

^bThe various reduced moduli considered are appropriate for contact between a Si probe and, respectively, a PMMA polymer sample, Douglas fir wood, plate glass, annealed bronze, Ge, Si, stainless steel, or diamond.

parameter, whereas **Figure 9** plots the JOA_i with respect to the corresponding Maugis lambda parameter. **Figure 9** may reasonably serve as a master curve for UFM contrast, although with some caveats, as discussed below. More generally, **Figures 8** and **9** together demonstrate nicely both the predictability and linearity of UFM contrast

- Reduced modulus (K , GPa)
- Adhesion energy (w , J m⁻²)
- ▲ Reduced radius (r , nm)
- ▼ AFM setpoint force (F , nN)
- ◆ Spring constant (k_c , nN nm⁻¹)

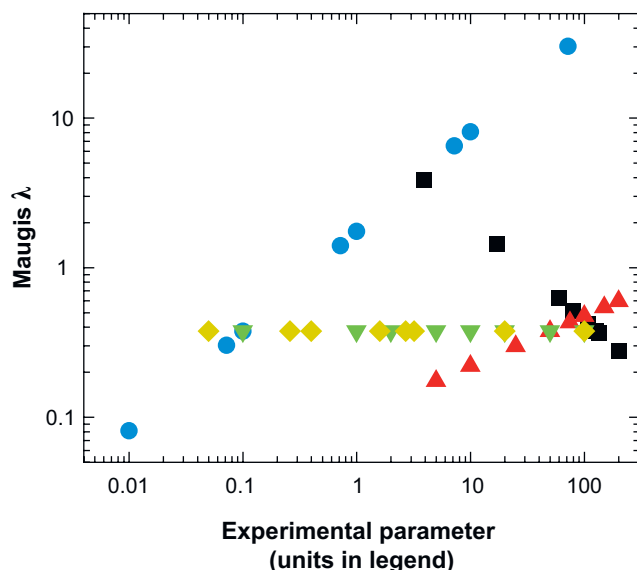


Figure 7

Maugis lambda term as a function of various experimental parameters, each independently calculated according to **Table 1**.

Figure 8

UFM jump-off amplitude for an increasing ultrasonic excitation (JOA_i) as a function of various experimental parameters.

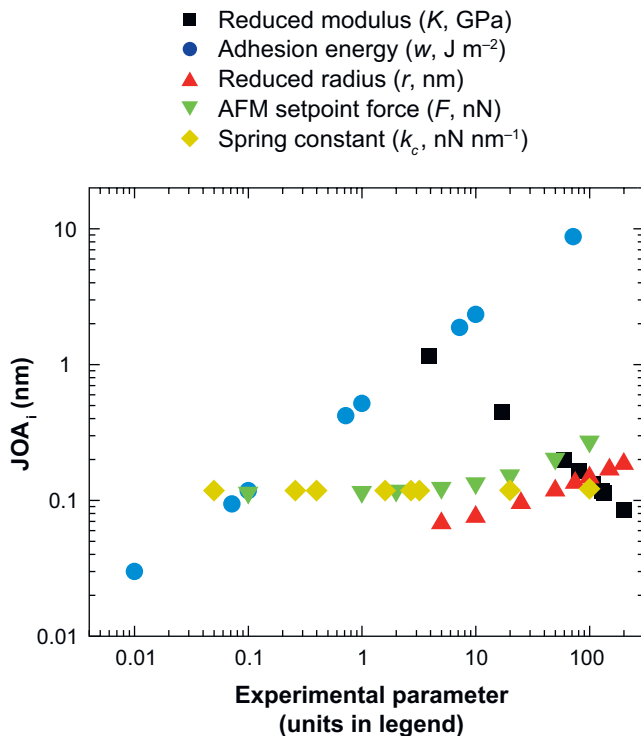
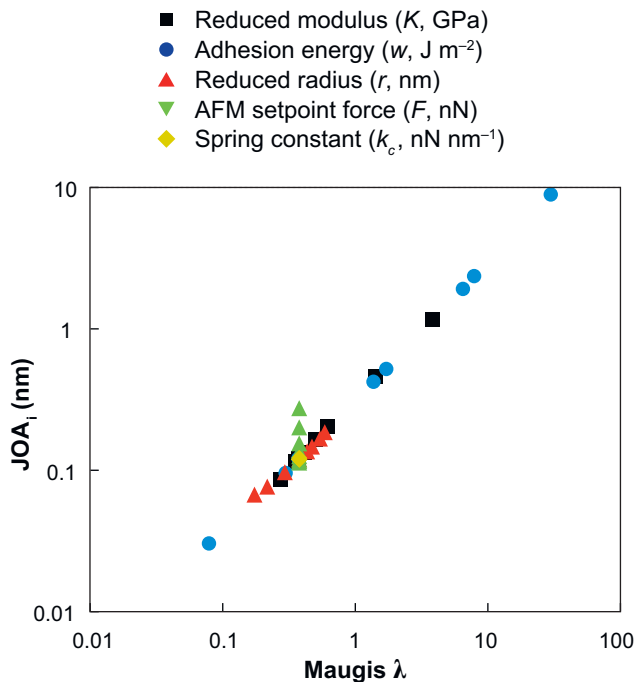


Figure 9

Increasing ultrasonic jump-off amplitude (JOA_i) as a function of Maugis lambda parameters, essentially replotting **Figure 8** with a redefined abscissa.



with respect to individual materials properties as well as the challenges in interpreting these UFM spectra for surfaces on which more than one property varies at a time.

The decrease in the characteristic JOA_i with an increase in the sample reduced modulus (K) is easy to understand because (a) the F - s curve is steep for a stiff material and slowly increases for a compliant sample; (b) for a given setpoint force, the initial indentation is therefore much larger for the compliant material; and thus (c) the ultrasonic amplitude necessary to overcome this indentation, so that the tip and sample lose contact each cycle, is evidently large compared with that required for a stiff F - s curve. Alternatively, the Maugis lambda parameter is inversely proportional to the reduced modulus (Equation 4), so that the JOA_i decreases further for stiff materials because the point at which contact is lost in the F - s curve approaches a separation of 0 (the bridging neck is not as extensive).

Increases in the adhesion energy and/or the reduced radius, in contrast, increase the JOA because these variations increase lambda and consequently the separation necessary to lose contact. There is also sensitivity to the initial AFM setpoint force because this increases the initial indentation, albeit weakly for relatively stiff materials. The spring constant remains unimportant at this stage because the contrast is essentially proportional to when a tip and sample lose contact, not how much the lever deflects as a result. This is significant because it implies that the absolute JOA_i in UFM spectra is lever independent, allowing quantitative comparisons between measurements performed with different cantilevers, laser alignments, etc.

UFM compliance mapping. Finally, the real advantage of UFM, the ability to map mechanical properties while scanning, incorporates one further complication: real-time signal analysis. This is generally achieved with a lock-in amplifier to sensitively record the amplitude and phase of UFM spectra excited at every pixel. The amplitude detected in this manner (LIA_r , where LIA denotes lock-in amplifier output) is loosely proportional to the integral of each UFM spectrum and thus increases strongly for ultrasonic amplitudes beyond the JOA_i . For a fixed excitation amplitude during scanning, the smaller the JOA_i , the larger the corresponding lock-in amplitude because the integral of the spectra is much larger when the tip loses contact early in each modulation. In other words, using the lock in provides UFM image contrast that is strongest for weak JOA_i , essentially a contrast inversion. This is demonstrated in **Figure 10**, which presents topography (**Figure 10**, left) and UFM LIA_r maps (**Figure 10**, right) of alumina spheres in a polymer matrix, in which the relatively stiff spheres (small JOA_i) yield bright UFM LIA_r contrast as compared with the surrounding compliant matrix (which exhibits a large JOA_i). In the simplest case, strong UFM LIA_r signals therefore correspond to increased surface stiffness, as expected from **Figure 8**.

This easy interpretation is complicated in two ways. First, because a lock in essentially integrates the UFM spectra, the imaging contrast is now also a function of the magnitude of the lever deflection and the modulation amplitude. This returns sensitivity to the value of the lever spring constant, practically requiring normalization for proper comparison between distinct measurements performed with new cantilevers or even with different laser alignments according to Equation 6. **Figure 11**

LIA: lock-in amplifier output (specifically the amplitude signal)

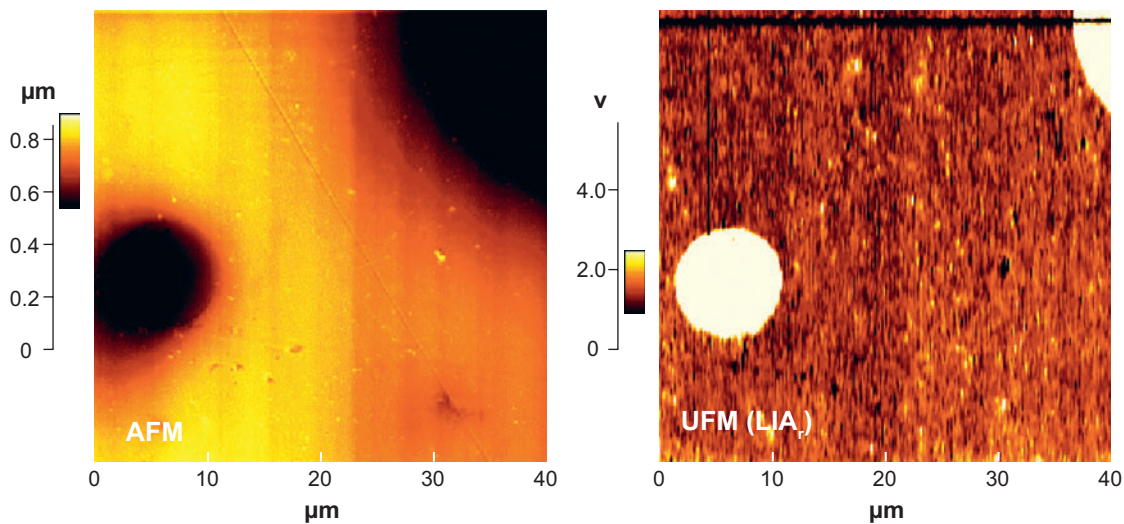


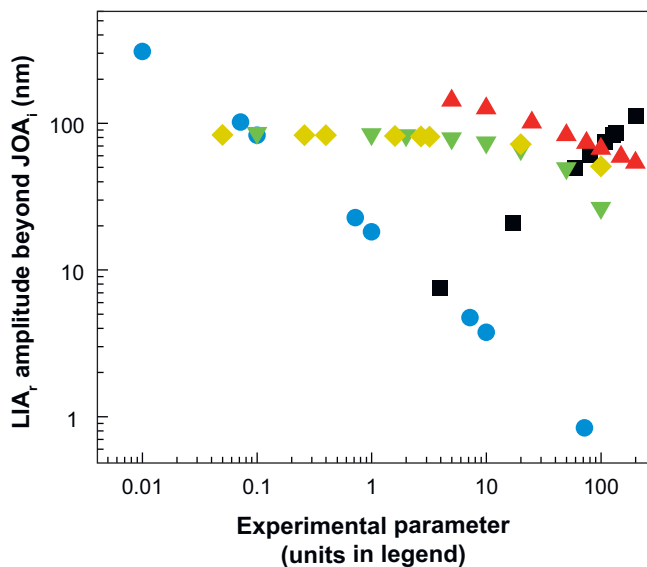
Figure 10

AFM topography (*left*) and UFM LIA_r image (*right*) for alumina spheres (bright contrast) embedded in a polymer matrix.

Figure 11

UFM image sensitivity (LIA_r) to the same experimental parameters as in Figures 7–9.

- Reduced modulus (K , GPa)
- Adhesion energy (w , $J\ m^{-2}$)
- ▲ Reduced radius (r , nm)
- ▼ AFM setpoint force (F , nN)
- ◆ Spring constant (k_c , $nN\ nm^{-1}$)



summarizes this point by presenting the theoretical UFM imaging contrast for the same parameters considered in **Figures 7–9**.

Figure 9 reveals an even greater challenge: UFM contrast is strictly sensitive to the collective properties of the sample (λ), not just one parameter such as the reduced modulus. And heterogeneous surfaces are seldom so convenient as to exhibit variations in only one term. As a result, quantifying the properties of one material or another can be a challenge because the LIA_r response for each may increase, decrease, or even remain constant depending on whether the modulus, adhesion, and curvature interact constructively or destructively. This is particularly true for UFM, as it is often performed with small contact setpoints on the order of tens of nano-Newtons, minimizing sample and tip damage. Strong UFM LIA_r signals thus may alternatively indicate a decrease in the local sample surface energy or in the radius of curvature.

UFM spectra hysteresis. One final point regarding UFM contrast is worth discussing. If the UFM spectra recorded during the decreasing portion of the ultrasonic modulation are compared with the increasing spectra, a hysteresis will always be noticed near the JOA (this is revealed by carefully inspecting **Figures 4–6**). Conceptually, this is because once the JOA_i is surpassed the lever deflects abruptly, shifting the tip position (d_a). Upon a decrease in the ultrasonic amplitude, this extra shift must be overcome before the tip and sample regain constant contact throughout each ultrasonic period. This jump-on amplitude for decreasing ultrasonic excitations (JOA_d) is thus always less than the JOA_i , nominally by the magnitude of the jump at the JOA_i itself. More importantly, beyond this omnipresent UFM hysteresis the exact positions of JOA_i and JOA_d and the magnitude of the jumps at these amplitudes are sensitive to the sample properties. **Figure 12** predicts the hysteresis area as a function of the same experimental parameters shown in **Figures 7–10**. Careful analysis of the data also reveals a kink in the responses for the reduced modulus and adhesion energy. This change in behavior corresponds to the onset of hysteresis in the simple contact adhesion, i.e., when the Maugis λ parameter exceeds 0.94 (cf. **Figure 7**), and therefore to an abrupt enhancement in the UFM hysteresis response. Such hysteretic signals have been considered by several authors (13–15).

UFM applications. On the basis of this careful analysis of UFM contrast, there may be concerns about the practicality of using this method. But bear in mind that the above discussions are presented to review all the known complications, whereas actual experimental results will often be sensitive primarily to far fewer (and controllable) details. Accordingly, a wide range of UFM measurements has been reported on polymers (16–18), metals (19, 20), semiconductors (21–23), ceramics (24–27), and a variety of nanomaterials (1, 28–30). Quantitatively, these studies are generally based on analyzing individual UFM spectra (especially the JOA_i and/or the hysteresis area) or differential UFM measurements (essentially comparing JOA_i for different setpoint forces). A general caveat for SPM property measurements still holds, though: Any comparisons are best performed in a single experimental session so as to minimize

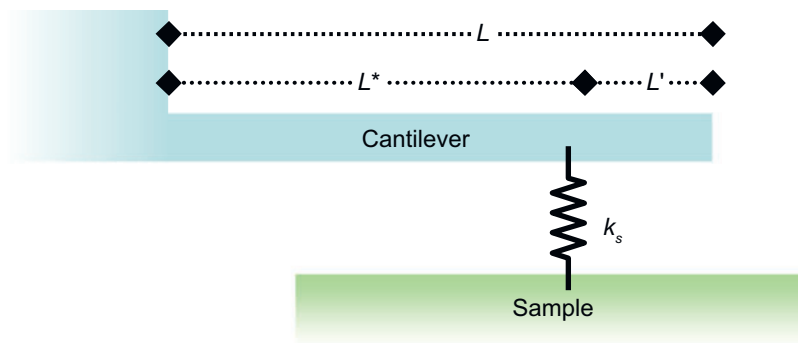


Figure 13

Sketch of an AFAM mechanical model, where k_s represents the contact stiffness and L , L^* , and L' denote the total lever length, distance from the lever base to the tip, and its complement, respectively.

Cantilever dynamics. A brief discussion of cantilever dynamics is crucial before AFAM contrast can be understood. Cantilevers naturally exhibit a resonant response with strong sensitivity to tip-sample force gradients. The first-mode free resonance (Equation 10) is thus often implemented in ac-AFM imaging modes. Higher-order modes are occasionally employed as well, providing the possibility of enhanced and/or simultaneous multiple signal detection (topography as well as magnetic or electronic imaging) (40–47).

$$\omega' = \omega_0 \sqrt{1 - \frac{F'}{k}}. \quad 10.$$

More important is that when the AFM probe is in strong contact with a surface (**Figure 13**), the various resonant frequency modes shift appreciably into the ultrasonic regime. The details are certainly a function of cantilever geometry (48, 49), which is of course fixed for a given measurement and similar for multiple measurements using similar levers. The crux of AFAM, though, is the far-more-significant sensitivity of these contact resonance frequencies to the contact stiffness with the surface (k_s), again providing contrast related to the shape of the force-separation curve.

Figure 14 presents the theoretical amplitude as a function of detection position along a lever, both for contact resonances of the first three vibrational modes and for several cases of contact stiffness, taken from Rabe et al. (50). **Figure 14** is especially significant because it indicates that the contact-resonant-amplitude signal will be strongest at certain positions, depending on the mode. Conversely, a null response can be obtained even during strong ultrasonic excitation and resonance if the AFM detection laser is aligned at a detection node (which is obviously to be avoided).

A seemingly complicated Equation 11 is necessary to describe the frequency for the contact resonance (f_n), which incorporates seven terms. These include a cantilever term that accounts for lever and tip geometry (c_B); a term related to the position of the tip along the lever (L^* , where L is the entire lever length and $L' = L - L^*$); the lever

basis of measuring the free-resonant frequencies ($f_{n,free}$) of each vibrational mode (n) and the established wavenumber values [k_n , where $k_1L = 1.8754$, $k_2L = 4.69409$, $k_3L = 7.85476$, etc. (50)]. Ultimately, the constant c_B should be independent of the wavenumber (n), providing a sanity check for a proper experimental setup.

$$c_B = \frac{k_n}{\sqrt{f_{n,free}}}. \quad 13.$$

Next, although the term L^* is described with respect to the position of the tip along the lever, this geometrically defined (or microscopically measured) value seldom provides the most accurate AFAM measurements. As a result, an additional calibration whereby L^* is numerically determined is generally performed in AFAM. This requires measuring the contact resonant frequency of at least two, if not more, distinct vibrational modes with otherwise the same experimental conditions (force, sample position, etc.). The contact stiffness (k_s) is then calculated (11) for each mode detected, each as a function of a range of practical L^*/L values, where c_B , f_n , and L' have been appropriately substituted. Because k_s should be the same for each of these measurements, L^* is then determined self-consistently, as indicated in **Figure 15**. This method also provides an indication of whether experimental data based on any particular vibrational mode are accurate. In the case of **Figure 15**, for example, the use of $L^* = 0.994$ will not produce reliable results for AFAM data acquired on the basis of the second resonant mode but is perfectly appropriate for first- and third-mode data.

For the most quantitative AFAM results, the L^* calibration step should be performed on both the sample of interest as well as a standard of similar mechanical properties. Furthermore, multiple recalibrations should also be performed during, and especially after, an AFAM experiment. This is to identify and account for drift and especially any abrupt changes in the L^* value, as may occur for changes in the tip shape, sample contamination, etc. In this manner, one can achieve mechanical resolution comparable to traditional macroscopic acoustic measurements as well as nanoindentation measurements, even for very thin films for which nanoindentation can be impractical (52, 53).

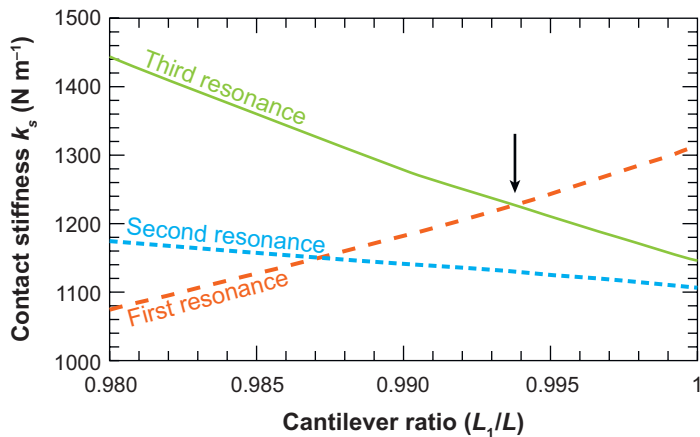


Figure 15

Calculated contact stiffness as a function of practical L^*/L values. From Kester et al. (39), p. 1275, with permission. Copyright 2000, Elsevier.

Moreover, performing multiple measurements on samples and on standards has an additional benefit for data analysis. In Equation 12, the sample mechanical properties depend sensitively on the reduced contact radius and the applied force, although these terms are difficult to know with sufficient precision and can change during a measurement. Equation 14 overcomes this limitation; an unknown reduced modulus is determined on the basis of the modulus of the reference standard as well as the contact stiffnesses of the unknown and the reference (both determined from the AFAM-derived contact resonant frequencies). The power m accounts for the tip geometry, equaling 1 for a flat punch and 3/2 for a spherical probe, and practically is usually somewhere in between. Using multiple references with moduli close to (and especially bracketing) that of the sample yields the best results (54).

$$K_s = K_{reference} \left(\frac{k_s}{k_{reference}} \right)^m. \quad 14.$$

AFAM mechanical measurements are generally performed in a point-by-point mode, gathering contact-resonant-frequency spectra at positions of interest on a sample and then calculating the reduced modulus as described above. Mapping such properties with AFM-like resolution is substantially more difficult and time consuming because of the large number of measurements that must be made (requiring amplitude detection for at least 50 distinct frequencies for 256×256 pixels), integration of the necessary external excitation and analysis hardware with the AFM system itself, and synching of each individual measurement with either a scanned or a pixel-by-pixel stepping mode. All these tasks must be completed uniformly without drift and without tip degradation over tens of minutes to more than an hour. Still, with some customization, pixel-by-pixel AFAM spectra have been acquired, allowing mapping in as fast as 15 min (55, 56). Another approach, which avoids pixel-by-pixel synching complications, instead simply integrates contact resonant spectra acquired continuously during scanning. This method, so-called contact acoustic resonance dispersive spectroscopy (CARDS) (D. Shuman & B. Huey, unpublished data), provides spectra of the contact resonance amplitude versus frequency that are representative of the mechanical properties for the entire surface imaged. The peak positions indicate the contact stiffness of the various surface components, whereas the integrated peak areas reveal aerial fractions of each component, analogous to X-ray or energy dispersive spectra.

AFAM compliance mapping. Finally, as with UFM, qualitative AFAM images can be rapidly acquired without requiring the above calibration steps. In this case, the sample or tip is driven ultrasonically but at a fixed frequency near the contact resonance for at least one surface component. Detecting the lever amplitude as a function of position (usually with a lock-in amplifier) thereby provides an AFAM compliance map that highlights a particular surface property or material. The contrast can be superb because the signal is a resonant peak, but there is also an important complication. As **Figure 16** demonstrates, the AFAM amplitude for a given excitation frequency, for example ω_0 , is strongest for material B, whereas the contrast is weak for both materials A and C, even though C is evidently the stiffest. This is quite distinct from

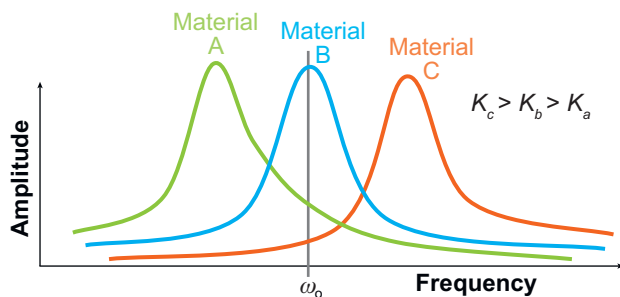


Figure 16

Contact resonant peaks (ω_0) shift with the contact stiffness (K) for three materials (A, B, C), providing a strong signal for one material (B) and weak contrast for the others (A and C), even though B is more compliant than C and less compliant than A.

UFM compliance maps, which yield contrast that is proportional to the local sample properties according to the generally consistent trends of **Figure 10**. To cope with this challenge, either multiple images must be acquired at distinct frequencies or precise contact resonance mapping experiments must be carried out as described above to determine the entire resonant curves for each material (or even for each position). The significance of possibly contraindicating experimental parameters, as discussed for UFM, has not yet been considered for AFAM.

AFAM applications. AFAM has been applied in various forms for studies of ceramics (57–59), clay (60, 61), polymers (62), and piezoelectric materials (thin film and bulk) (47, 63–67). As with UFM, measurements have been conducted as a function of depth (68–71) and of humidity (72). Unlike UFM, though, AFAM is inherently less sensitive to adhesive forces and capillarity because of the comparatively high contact forces necessary for consistent results. These are on the order of several hundred nano-Newtons to a few micro-Newtons, as opposed to UFM, which operates sufficiently down to a few nano-Newtons of force. Such high loads have an obvious drawback in that they often lead to significant tip wear. Conveniently, however, the flat-punch-like geometry of most tips that eventually develops (sometimes even in seconds) is both easier to model mechanically and mechanically more stable (73–75).

Other Variations

There are a host of related ultrasonic methods, each with their own advantages and challenges. Two of the earliest are scanning local acceleration microscopy (SLAM) (76) and scanning microdeformation microscopy (SMM) (77). Scanning tunneling microscopes have even been implemented to detect the near-field acoustic signals

HS-SPM: high-speed surface property mapping

(78, 79). There have also been several intriguing efforts to operate at higher frequencies; such approaches generally incorporate heterodyne methods (80, 81), essentially leveraging the nonlinear tip-sample coupling to generate difference frequency signals that are compatible with the bandwidth of typical lock-in amplifiers. These methods maintain the phase relationship between the driving and detection signals and therefore provide the possibility for time-resolved (and hence depth-dependent) studies.

Moreover, ultrasonic methods are increasingly being employed to detect properties other than just mechanics, such as thermal, electronic, or piezoelectric effects. Significant work recently has been conducted along these lines to study ferroelectric and piezoelectric materials (see, for example, References 10, 47, 67, and 82). Instead of actuating the sample with a transducer, however, one applies a bias to the AFM tip, which causes the sample beneath the probe to act as a local transducer (the samples are piezoelectric, after all). These methods are therefore extremely sensitive to not only mechanical contrast but the piezoelectric properties of the sample, their distribution, and even domain orientations beneath the probe.

Finally, ultrasonic AFM applications to biological, molecular, and medical studies (83, 84) are a natural direction for future measurements owing to the already pervasive use of ultrasound in these disciplines. As an example, Shekhawat & Dravid (83) demonstrated exceptional contrast for malaria parasites in red blood cells in air. UFM has even been performed *in vitro* by B. Huey, S. Kasas, & A. Kulik (unpublished data), although this is complicated by the transmission of ultrasound through fluids and therefore by the potential for long-range coupling between the vibrating sample and the entire cantilever (not just the tip). Even so, nanoscale compliance maps have been achieved for fixed nerve cells in solution, as revealed in the right panel of **Figure 17**, which includes the corresponding topography in the left panel for comparison.

NEXT STEPS

Ultrasonic applications of AFM are now firmly established as excellent techniques for nanomechanical measurements. Further work is still necessary to standardize the method for more widespread application, however. Particular challenges that remain include the incorporation of humidity and/or viscoelastic properties into the contrast theories, standardized and simple experimental procedures for quantitative results, and especially tip/cantilever optimization. Even more exciting, though, is the possibility to extend the benefits of acoustic methods into new areas of research beyond those already identified above. Two examples are presented in the rest of this section: high-speed surface property mapping (HS-SPM) and four-dimensional scanning probe microscopy (4d-SPM).

HS-SPM

A new advance in AFM builds upon two key aspects of AFAM to allow HS-SPM. First, because the various contact resonances employed for AFAM are at higher frequencies than the free resonances used for traditional AFM (up to an order of magnitude or

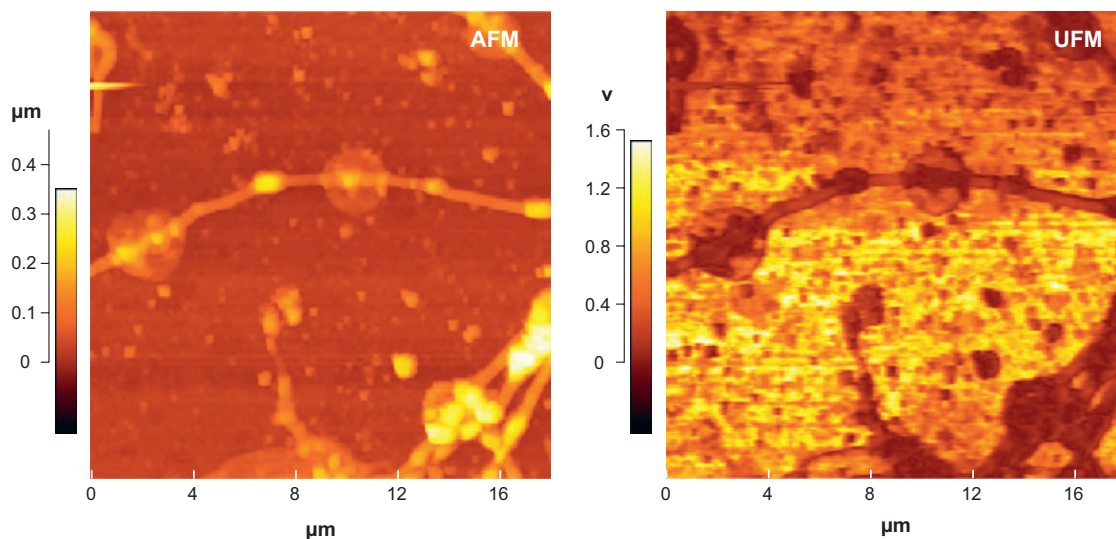


Figure 17

In vitro UFM exhibiting mechanical contrast for fixed nerve cells in solution (*right*) that appear as protruding lines in the topographic image at left.

more), the scanning speed can conceivably be increased as well without sacrificing resolution. Traditional AFM is usually operated at line rates of approximately 1 Hz; in HS-SPM, an equivalent number of tip-sample interactions per pixel is evidently achieved with at least 10-Hz line rates. Through the use of commercially available lock-in hardware dedicated for rapid and low signal-to-noise detection, scanning up to 100 Hz still provides sufficient resolution, with 40 interactions (periods) per pixel, assuming 256 pixels per line scan and a 2-MHz contact resonance (each pixel requires 20 μs in this case, as the tip traverses the surface in both directions every 10 ms). This amounts to complete image frames (256 \times 256 pixels) in 2.56 s. For scan sizes of 20 μm , this amounts to tip speeds of 4 mm s^{-1} . In unpublished work by R. Nath & B. Huey, images at tip speeds up to nearly 2 cm s^{-1} were even acquired in this manner, and frame rates of less than a second for nonsquare images were achieved. For a 256 \times 32-pixel rectangular image swath, for example, perfectly sufficient for monitoring a particular sample region or process, new images can be obtained in less than 1/3 of a second.

There are three caveats to this concept. First, AFM scanners are not designed for such high-speed actuation, particularly the vertical piezo. The effective mass of the z-piezo stack and AFM head is simply too large for most z-scanners to allow fast enough actuation to track a surface at 100 Hz. Additionally, high-frequency resonances may be established in the scanning head at these rates, which interfere with high-speed imaging. As a result, the essential aspect of nearly all modern AFM systems—the maintenance of a constant interaction force or force gradient during imaging (the setpoint)—cannot be achieved at high speeds with standard AFM systems.

Nevertheless, many early SPM systems and, even today, some high-resolution SPM imaging do operate sufficiently in the constant-height mode whereby the tip is simply rastered in a plane and the resulting interactions are merely recorded as a function of position. For contact AFM operated in this manner, the tip thus experiences higher forces upon encountering a protrusion and experiences lower forces for depressions, with corresponding increases or decreases, respectively, in the instantaneous lever deflection.

For high-speed scanning using contact resonances as implemented here, this necessary variation in force applied to the sample does not necessarily hinder amplitude or phase contrast. This is because the contact resonance, and thus the phase or amplitude detected for a fixed frequency near this resonance, shifts only subtly with applied force as compared with changes due to variations in contact stiffness. Of course, surface damage is possible, but, as long as the spring constant is sufficiently soft that the force variations are minimal, sample damage is limited. Indeed, both commercial and custom levers have been applied during scanning with 30–100-Hz line rates on surfaces ranging from polymers to metals to semiconductors, without significant surface modification. As a result, reasonable images of surface heterogeneities can be acquired at high image rates and high tip scanning speeds.

For example, **Figure 18b** presents a HS-SPM image of bacterial membrane fragments (wild-type bacteriorhodopsin) on a glass substrate, acquired in 16 s (B. Huey & J. Stuart, unpublished work). The membranes are roughly 5 nm thick and are substantially more compliant than the adjacent glass. If UFM imaging were employed, contrast would be dark when the tip contacted the soft membranes as opposed to the substrate. But for AFAM imaging, the contrast depends on the imaging frequency and its proximity to the contact resonances for each material. The images shown here are acquired in AFAM mode at the contact resonance of the membranes so

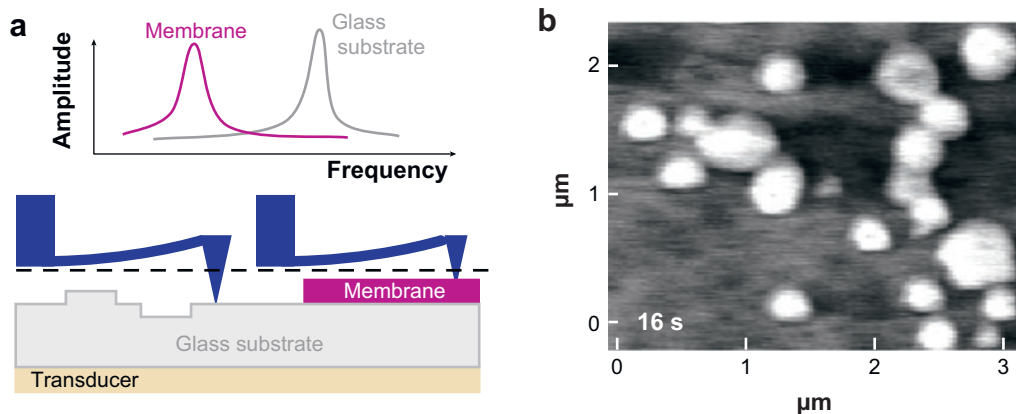


Figure 18

(a) Sketch of the principle behind AFAM-based high-speed surface property mapping (HS-SPM) showing contact resonance spectra varying strongly with material compliance but weakly with topography. (b) A compliance image of 5-nm-high bacteriorhodopsin membrane fragments acquired in just 16 s.

that they appear bright; in other words, when the tip contacts these protrusions, the amplitude actually increases. This is an important detail, as the tip amplitude is not merely clipped when colliding with the membranes at these high speeds. Imaging at the contact resonance for the substrate would invert the contrast, whereas imaging far from either contact resonance yields little contrast, as expected.

Many commercial AFM systems are not presently designed for such high-bandwidth-signal detection or recording. This may be overcome by modifications to existing hardware and software and, in the future, by system redesign as AFM manufacturers introduce new microscope platforms leveraging this notion. Indeed, several systems have already been commercially implemented for moderate improvements in speed (up to 10-Hz line rates). Torsional mode imaging, one such example, also employs a higher-frequency tip-surface interaction, in this case the torsional lever resonance. For substantially higher rate scanning, up to two orders of magnitude faster, a select few, highly specific, custom-designed systems employing specialty probes, actuation, and detection have been implemented, although these primarily target high-resolution applications and thus small (submicron) scan areas (85–98). One commercial system, presently available for larger areas, demonstrates video-rate (30 frames per second) capabilities for scan sizes up to approximately 20×20 microns, although only lever deflection is tracked and thus topography is primarily imaged (99, 100). However, none of these established systems leverage either the inherent speed advantages of contact resonances or the more substantial benefit of acoustic and AFM methods, i.e., local and even subsurface mechanical contrast.

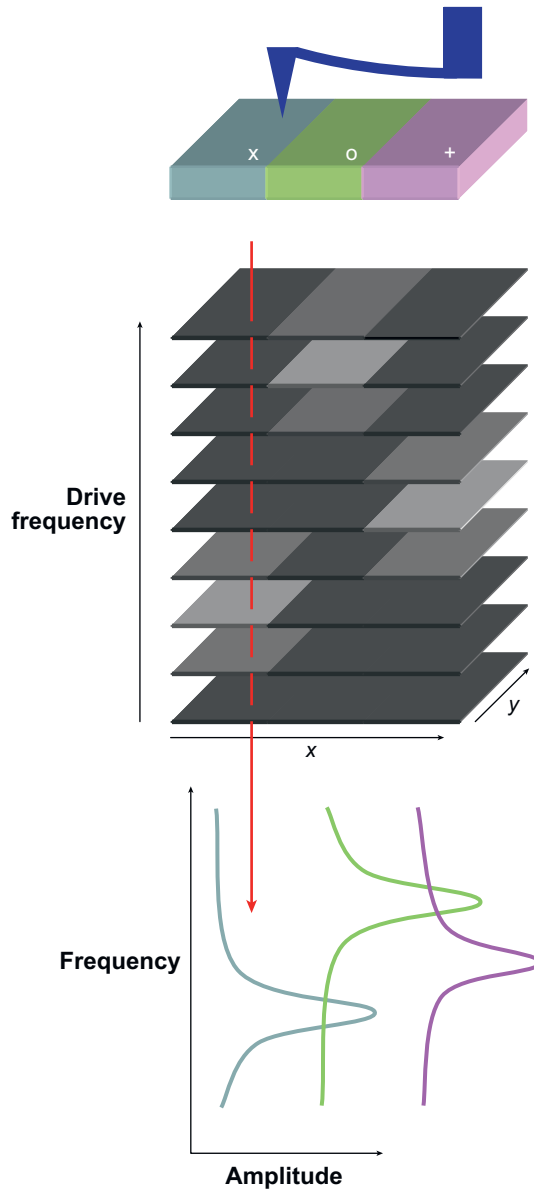
One drawback of HS-SPM is that quantitative results of surface mechanical properties will certainly be hindered by the additional error caused by any force variations during imaging. High-precision measurements can always be performed at slower speeds, though, once regions of interest are identified efficiently with HS-SPM. Practically, simply identifying regions of distinct properties and their spatial distribution is often sufficient in any case, as evidenced by the profound application of intermittent-contact phase imaging in the polymers discipline, despite the tremendous difficulties in accurately relating such images to quantitative surface properties. In this regard, HS-SPM is in some ways a higher-speed version of that very successful technology. HS-SPM may therefore have important implications for the further industrial acceptance and applications of AFM technology, in which speed is a primary limitation and indeed has improved little in the past 20 years.

4D-SPM

The advent of rapid imaging through HS-SPM or similar methods has further allowed nanoscale imaging with an effective fourth dimension (e.g., time, voltage, contact resonant frequency, or position), similar to concepts regularly applied in confocal optical microscopy. This has obvious applications for AFAM: Consecutive images may be acquired at incremental excitation frequencies to efficiently build volumes of data “slices.” The data may then be mined in this fourth dimension to obtain contact resonant peak spectra for every point in an image, as sketched in **Figure 19**. This has significant advantages over pixel-by-pixel resonant frequency sweeping, including

Figure 19

4d-SPM schematic leveraging consecutive AFAM images with increasing ultrasonic drive frequencies to allow rapid contact resonance mapping by “drilling through” the volume of image slices.



higher speed; a corresponding lower sensitivity to thermal drift; simpler implementation; and especially the ability to easily apply already established routines for analyzing confocal imaging slices, such as drift correction, volumetric analysis and visualization, any-dimensional sectioning, and feature tracking.

As an example, 4d-SPM was performed in AFAM mode at the lithographically defined edge of a 120-nm-thick Au thin film on a silicon substrate. A volume of

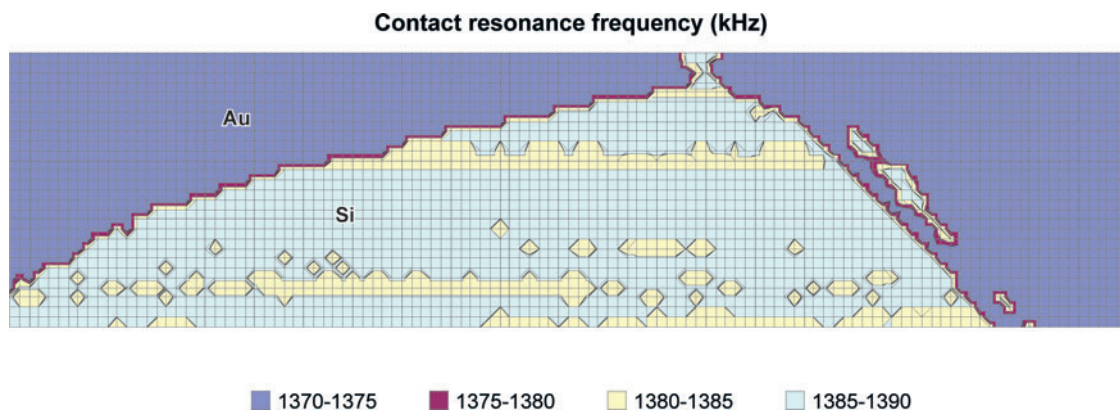


Figure 20

Contact resonance map (40-nm pixels) extracted from a 4-d-SPM volume of 100 distinct AFAM images at the edge of a 120-nm-thick Au film on Si.

100 images, each acquired in less than 30 s and at 1-kHz excitation frequency increments, thereby records the resonant spectra at each pixel with high spatial resolution (each pixel is <40 nm on a side). **Figure 20** presents the easily extracted contact resonant frequency for each pixel, identifying the Si and Au with high signal-to-noise resolution. This concept has the additional obvious benefit that it can be coupled with HS-SPM for particularly rapid, and quantitative, surface property analyses.

Of course, imaging simply as a function of position or time is possible as well. High-resolution, large-area imaging becomes practical using simple step-and-repeat schemes. Through the use of either built-in or custom-added lateral actuators, surface property maps can be rapidly collected from adjacent sample regions and eventually stitched together. Imaging a single area as a function of time, in contrast, will allow dynamic processes to be monitored. This is demonstrated by the series of phase images in **Figure 21** by R. Nath & B. Huey (unpublished data), which are extracted from **Supplemental Video 1** (follow the Supplemental Material link from the Annual Reviews home page at <http://www.annualreviews.org>). A movie of simultaneously acquired amplitude images is also available online (**Supplemental Video 2**). **Supplemental Video 1** and derived images (**Figure 21**) display the piezoactuation phase response for developing domains in a ferroelectric thin film (PZT). These images were acquired by applying an AC bias to a conducting AFM tip, which causes the ferroelectric material beneath the probe to piezoactuate in phase for domains oriented in one direction and out of phase for domains oriented in the other direction. In this case HS-SPM was employed as well such that distinct images were acquired at 1.5-s intervals. 4-d AFM thus allowed the nucleation and growth of oriented ferroelectric domains to be visualized with otherwise inaccessible spatial and temporal resolution. Volumes of voltage dependencies can be acquired in the same slice-by-slice manner, for example, to provide rapid, high-resolution maps of piezoelectric hysteresis loops (N. Polomoff & B. Huey, unpublished data). As AFM imaging speeds continue to increase, such novel dynamic measurements will become increasingly feasible.

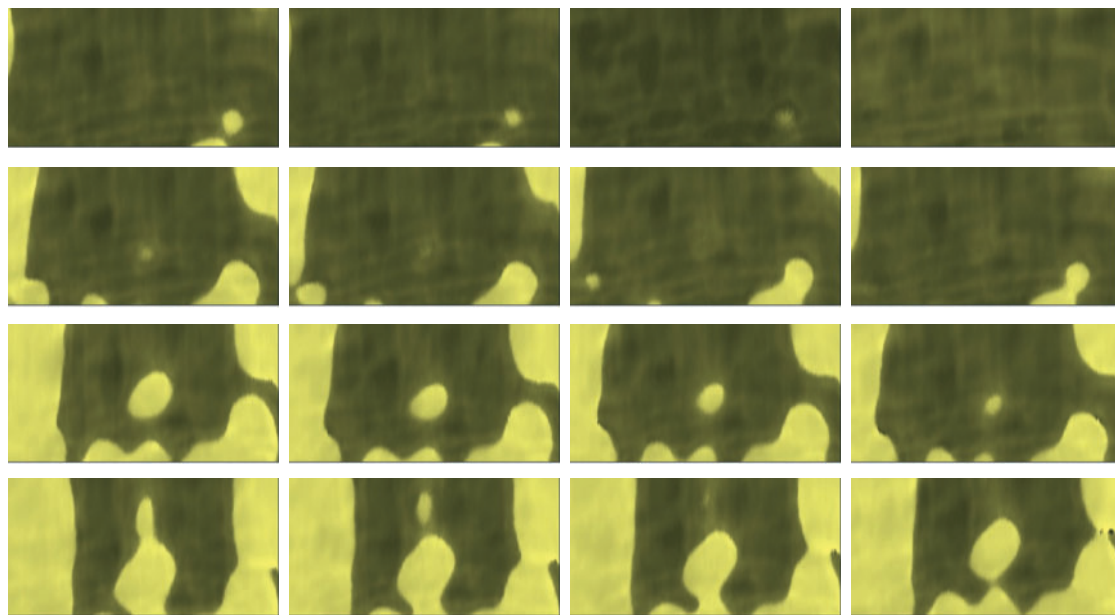


Figure 21

HS-SPM images revealing ferroelectric domain wall motion, each acquired in just 1.5 s and measuring 1.4 by 1 μm (frames extracted from **Supplemental Video 1**).

CONCLUSION

Acoustic and AFM methods clearly provide superb mechanical resolution of nanoscale features. Impressive quantitative and numerous qualitative results have been reported with several variations of these methods, particularly UFM and AFAM. In the case of UFM, usually applied with a relatively low contact force (<100 nN), the contrast results from a MHz-range tip-sample indentation modulated to a kHz-range signal for detection. The average force experienced by the probe during this amplitude modulation, the so-called UFM spectra, is sensitive to the shape of the force-indentation-retraction curve, which itself is a function of the surface mechanical properties. AFAM, in contrast, derives its surface stiffness sensitivity from shifts in the resonance of a tip/cantilever in somewhat more rigid contact with a sample (>100 nN). These contact resonances provide a ready numerical method for quantifying the contact stiffness. In either case, additional sensitivity to adhesion energy, tip radius, and lever spring constant has also been reported, unfortunately sometimes as contraindicating factors. Finally, leveraging the concepts of ultrasonic and AFM methods has uniquely allowed the development of high-speed methods such as HS-SPM and 4d-SPM, providing images with mechanical or electromechanical contrast hundreds of times faster than can conventional SPM measurements. This new application of ultrasonic and AFM concepts provides numerous possibilities for novel quantitative measurements, rapid large area scanning, and surface dynamics studies, all with nanoscale resolution.

SUMMARY POINTS

Ultrasonic and AFM methods are

1. rooted in contact mechanics and beam dynamics;
2. sensitive to nanoscale mechanical properties (and others), including local stiffness and adhesion, in a predictable manner;
3. capable of resolving both surface and buried structures;
4. applicable to a wide range of materials (ceramics, metals, polymers, biological substances);
5. most easily applied for the qualitative identification, mapping, and characterization of distributions of surface heterogeneities;
6. applicable for quantitative measurements with appropriate calibrations; and
7. enabling novel capabilities, including high-speed surface property mapping (HS-SPM).

FUTURE ISSUES

Next-generation challenges and opportunities in acoustics and AFM will emphasize

1. AFM system design (lower noise, higher bandwidth detection),
2. cantilever design (optimized for contact resonance detection),
3. tip design (sharp yet robust),
4. the separation of contraindicating stiffness versus adhesion effects,
5. the simplification and commercialization of methods/analyses,
6. in vitro operation,
7. subsurface feature detection and quantification, and
8. high-speed characterization and mapping.

ACKNOWLEDGMENTS

Useful discussions with O. Kolosov, G.A.D. Briggs, A. Kulik, N. Burnham, W. Arnold, U. Rabe, J. Turner, and D. Hurley are appreciated. The assistance of M. Zhao, R. Nath, and D. Shuman in preparing this manuscript is noted. Support is provided by NSF-ENG-CMS-NBM-0626231 and the University of Connecticut Research Foundation.

LITERATURE CITED

1. Bonnell DA, Huey BD. 2001. Basic principles of scanning probe microscopy. In *Scanning Probe Microscopy & Spectroscopy: Theory, Techniques, and Applications*, ed. DA Bonnell, pp. 7–42. New York: Wiley-VCH
2. Briggs A, Kolosov O. 1998. Anisotropic elastic characterization of surfaces from 2 MHz to 20 GHz. *Ultrasonics* 36:317–21
3. Kolosov O, Yamanaka K. 1993. Nonlinear detection of ultrasonic vibrations in an atomic force microscope. *Jpn. J. Appl. Phys. Pt. 2* 32:L1095–98
4. Yamanaka K, Ogiso H, Kolosov O. 1994. Ultrasonic force microscopy for nanometer resolution subsurface imaging. *Appl. Phys. Lett.* 64:178–80
5. Rabe U, Arnold W. 1994. Acoustic microscopy by atomic-force microscopy. *Appl. Phys. Lett.* 64:1493–95
6. Burnham NA, Kulik AJ. 1999. *Surface Forces and Adhesion*. New York: CRC Press
7. Johnson KL, Kendall K, Roberts AD. 1971. Surface energy and the contact of elastic solids. *Proc. R. Soc. London Ser. A* 324:301–13
8. Johnson KL. 1985. *Contact Mechanics*. Cambridge, UK: Cambridge Univ. Press
9. Maugis D. 1992. Adhesion of spheres: the JKR-DMT transition using a dugdale model. *J. Colloid Interface Sci.* 150:243–69
10. Huey BD. 2004. Nanometer scale measurement and control of ferroelectric polarization at MHz frequencies. In *Nanoscale Phenomena in Ferroelectric Thin Films*, ed. S Hong, pp. 239–62. New York: Kluwer
11. Dinelli F, Castell MR, Ritchie DA, Mason NJ, Briggs GAD, Kolosov OV. 2000. Mapping surface elastic properties of stiff and compliant materials on the nanoscale using ultrasonic force microscopy. *Philos. Mag. A* 80:2299–323
12. Muthuswami L, Geer RE. 2004. Nanomechanical defect imaging in premetal dielectrics for integrated circuits. *Appl. Phys. Lett.* 84:5082–84
13. Inagaki K, Matsuda O, Wright OB. 2002. Hysteresis of the cantilever shift in ultrasonic force microscopy. *Appl. Phys. Lett.* 80:2386–88
14. Szoszkiewicz R, Bhushan B, Huey BD, Kulik AJ, Gremaud G. 2005. Correlations between adhesion hysteresis and friction at molecular scales. *J. Chem. Phys.* 122:144708
15. Szoszkiewicz R, Bhushan B, Huey BD, Kulik AJ, Gremaud G. 2006. Adhesion hysteresis and friction at nanometer and micrometer lengths. *J. Appl. Phys.* 99:014310
16. Iwata F, Suzuki Y, Moriki Y, Koike S, Sasaki A. 2001. Nanowearing property of a fatigued polycarbonate surface studied by atomic force microscopy. *J. Vac. Sci. Technol. B* 19:666–70
17. Porfyrakis K, Assender HE, Robinson IM. 2002. The interrelationship between processing conditions, microstructure and mechanical properties for injection moulded rubber-toughened poly(methyl methacrylate) (RTPMMA) samples. *Polymer* 43:4769–81
18. Onaran AG, Balantekin M, Lee W, Hughes WL, Buchine BA, et al. 2006. A new atomic force microscope probe with force sensing integrated readout and active tip. *Rev. Sci. Instrum.* 77:023501

19. Druffner CJ, Schumaker EJ, Murray PT, Sathish S. 2003. *Imaging the microstructure of copper with the atomic force microscope (AFM) and ultrasonic force microscope (UFM)*, 122. San Diego, CA: SPIE
20. Kuhr SJM, Pinnell MF, Eylon D. 2003. *Microstructural study of nano-precipitates in RRA treated Al-7075 T6 using AFM/UFM/STEM*, 73. San Diego, CA: SPIE
21. Shekhawat GS, Kolosov OV, Briggs GAD, Schaffer EO, Martin S, Geer RE. 2001. *Nanoscale elastic imaging of aluminum/low- k dielectric interconnect structures*, 1. San Francisco, CA: Mater. Res. Soc.
22. Geer RE, Kolosov OV, Briggs GAD, Shekhawat GS. 2002. Nanometer-scale mechanical imaging of aluminum damascene interconnect structures in a low-dielectric-constant polymer. *J. Appl. Phys.* 91:4549–55
23. Muthuswami L, Zheng Y, Geer RE. 2003. *Nondestructive nanomechanical imaging: cross-sectional ultrasonic force microscopy of integrated circuit test structures*, 54. San Diego, CA: SPIE
24. Grier EJ, Kolosov O, Petford-Long AK, Ward RCC, Wells MR, Hjorvarsson B. 2000. Structural changes to epitaxial (0001) holmium layers during hydrogen loading. *J. Phys. D* 33:894–900
25. Altemus B, Shekhawat G, Bai X, Geer RE, Castracane J. 2001. *Nanoscale elastic imaging of micro-electro-mechanical system based micromirrors*, 143. San Francisco, CA: SPIE
26. Druffner CJ, Sathish S. 2003. Atomic force and ultrasonic force microscopic investigation of laser-treated ceramic head sliders. *J. Am. Ceram. Soc.* 86:2122–28
27. Gill VS, Hallinan KP, Brar NS. 2005. *Nanocharacterization of bio-silica using atomic force and ultrasonic force microscopy*, 751. Singapore: SPIE
28. Kolosov OV, Castell MR, Marsh CD, Briggs GAD, Kamins TI, Williams RS. 1998. Imaging the elastic nanostructure of Ge islands by ultrasonic force microscopy. *Phys. Rev. Lett.* 81:1046–49
29. Muthuswami L, Ajayan PM, Geer RE. 2003. Nanomechanical imaging of multi-walled carbon nanotubes. In *Microscopy of Semiconducting Materials 2003*, pp. 633–36. Philadelphia: Inst. Phys.
30. Yuegui Z, Geer RE. 2004. *Nondestructive mechanical imaging of SnO₂ nanobelts*, 14. San Diego, CA: SPIE
31. Yamanaka K, Ogiso H, Kolosov O. 1994. Analysis of subsurface imaging and effect of contact elasticity in the ultrasonic force microscope. *Jpn. J. Appl. Phys. Pt. 1* 33:3197–203
32. Chekanov AS, Low TS, Alli S, Kolosov O, Briggs A. 1996. *Microcracks of the thin-film head alumina*, 3696. Seattle: IEEE
33. Geisler H, Hoehn M, Rambach M, Meyer MA, Zschech E, et al. 2001. Elastic mapping of sub-surface defects by ultrasonic force microscopy: limits of depth sensitivity. In *Microscopy of Semiconducting Materials 2001*, pp. 527–30. Philadelphia: Inst. Phys.
34. McGuigan AP, Huey BD, Briggs GAD, Kolosov OV, Tsukahara Y, Yanaka M. 2002. Measurement of debonding in cracked nanocomposite films by ultrasonic force microscopy. *Appl. Phys. Lett.* 80:1180–82

35. Sarioglu AF, Atalar A, Degertekin FL. 2004. Modeling the effect of subsurface interface defects on contact stiffness for ultrasonic atomic force microscopy. *Appl. Phys. Lett.* 84:5368–70
36. Tsuji T, Irihama H, Mihara T, Yamanaka K. 2004. Imaging and evaluation of nano-scale crack by using ultrasonic atomic force microscopy. In *Advances in Fracture and Failure Prevention, Pts. 1 and 2*, pp. 1067–72. Stäfa-Zürich: Transtech Publ.
37. Turner JA, Hirsekorn S, Rabe U, Arnold W. 1997. High-frequency response of atomic-force microscope cantilevers. *J. Appl. Phys.* 82:966–79
38. Rabe U, Kester E, Arnold W. 1999. Probing linear and non-linear tip-sample interaction forces by atomic force acoustic microscopy. *Surf. Interface Anal.* 27:386–91
39. Kester E, Rabe U, Presmanes L, Tailhades P, Arnold W. 2000. Measurement of Young's modulus of nanocrystalline ferrites with spinel structures by atomic force acoustic microscopy. *J. Phys. Chem. Solids* 61:1275–84
40. Martin Y, Williams CC, Wickramasinghe HK. 1987. Atomic force microscope-force mapping and profiling on a sub 100-Angstrom scale. *J. Appl. Phys.* 61:4723–29
41. Ducker WA, Cook RF. 1990. Rapid measurement of static and dynamic surface forces. *Appl. Phys. Lett.* 56:2408–10
42. Hillenbrand R, Stark M, Guckenberger R. 2000. Higher-harmonics generation in tapping-mode atomic-force microscopy: insights into the tip-sample interaction. *Appl. Phys. Lett.* 76:3478–80
43. Sahin O, Atalar A. 2001. Simulation of higher harmonics generation in tapping-mode atomic force microscopy. *Appl. Phys. Lett.* 79:4455–57
44. Ulcinas A, Snitka V. 2001. Intermittent contact AFM using the higher modes of weak cantilever. *Ultramicroscopy* 86:217–22
45. Stark R, Schitter G, Stark M, Guckenberger R, Stemmer A. 2004. State-space model of freely vibrating and surface-coupled cantilever dynamics in atomic force microscopy. *Phys. Rev. B* 69:5412
46. Crittenden S, Raman A, Reifenberger R. 2005. Probing attractive forces at the nanoscale using higher-harmonic dynamic force microscopy. *Phys. Rev. B* 72:1–13
47. Shin J, Rodriguez BJ, Baddorf AP, Thundat T, Karapetian E, et al. 2005. Simultaneous elastic and electromechanical imaging by scanning probe microscopy: theory and applications to ferroelectric and biological materials. *J. Vac. Sci. Technol. B* 23:2102–8
48. Shen KZ, Hurey DC, Turner JA. 2004. Dynamic behavior of dagger-shaped cantilevers for atomic force microscopy. *Nanotechnology* 15:1582–89
49. Muraoka M. 2005. Sensitivity-enhanced atomic force acoustic microscopy with concentrated-mass cantilevers. *Nanotechnology* 16:542–50
50. Rabe U, Janser K, Arnold W. 1996. Vibrations of free and surface-coupled atomic force microscope cantilevers: theory and experiment. *Rev. Sci. Instrum.* 67:3281–93

51. Rabe U, Amelio S, Kester E, Scherer V, Hirsekorn S, Arnold W. 2000. Quantitative determination of contact stiffness using atomic force acoustic microscopy. *Ultrasonics* 38:430–37
52. Hurley DC, Wiehn JS, Turner JA, Rice P. 2002. *Quantitative elastic-property information with acoustic AFM: measurements and modeling*, 65. San Diego, CA: SPIE
53. Hurley DC, Geiss RH, Kopycinska-Muller M, Muller J, Read DT, et al. 2005. Anisotropic elastic properties of nanocrystalline nickel thin films. *J. Mater. Res.* 20:1186–93
54. Hurley DC, Shen K, Jennett NM, Turner JA. 2003. Atomic force acoustic microscopy methods to determine thin-film elastic properties. *J. Appl. Phys.* 94:2347–54
55. Fukuda K, Irihama H, Tsuji T, Nakamoto K, Yamanaka K. 2003. Sharpening contact resonance spectra in UAFM using Q-control. *Surf. Sci.* 532:1145–51
56. Hurley DC, Kopycinska-Muller M, Kos AB, Geiss RH. 2005. Nanoscale elastic-property measurements and mapping using atomic force acoustic microscopy methods. *Meas. Sci. Technol.* 16:2167–72
57. Kester E, Rabe U, Presmanes L, Tailhades P, Arnold W. 1999. Measurement of mechanical properties of nanoscaled ferrites using atomic force microscopy at ultrasonic frequencies. *Nanostruct. Mater.* 12:779–82
58. Kassavetis SN, Logothetidis S, Matenoglou GM. 2006. Near-surface mechanical properties and surface morphology of hydrogenated amorphous carbon thin films. *Surf. Coatings Technol.* 200:6400–4
59. Passeri D, Bettucci A, Germano M, Rossi M, Alippi A, et al. 2006. Local indentation modulus characterization of diamondlike carbon films by atomic force acoustic microscopy two contact resonance frequencies imaging technique. *Appl. Phys. Lett.* 88:121910
60. Prasad M, Kopycinska M, Rabe U, Arnold W. 2002. Measurement of Young's modulus of clay minerals using atomic force acoustic microscopy. *Geophys. Res. Lett.* 29:1172–79
61. Vanorio T, Prasad M, Nur A. 2003. Elastic properties of dry clay mineral aggregates, suspensions and sandstones. *Geophys. J. Int.* 155:319–26
62. Preghenella M, Pegoretti A, Migliaresi C. 2006. Atomic force acoustic microscopy analysis of epoxy-silica nanocomposites. *Polym. Testing* 25:443–51
63. Rabe U, Kopycinska M, Hirsekorn S, Saldana JM, Schneider GA, Arnold W. 2002. High-resolution characterization of piezoelectric ceramics by ultrasonic scanning force microscopy techniques. *J. Phys. D* 35:2621–35
64. Kopycinska M, Ziebert C, Schmitt H, Rabe U, Hirsekorn S, Arnold W. 2003. Nanoscale imaging of elastic and piezoelectric properties of nanocrystalline lead-calcium titanate. *Surf. Sci.* 532:450–55
65. Jesse S, Baddorf AP, Rodriguez BJ, Gruverman A, Kalinin SV. 2005. *Imaging bio-electro-mechanics with scanning probe microscopy: unveiling nature's nanoscale form and function*, 67. Anaheim: Nano Sci. Technol. Inst.
66. Karapetian E, Kachanov M, Kalinin SV. 2005. Nanoelectromechanics of piezoelectric indentation and applications to scanning probe microscopies of ferroelectric materials. *Philos. Mag.* 85:1017–51

67. Zeng HR, Yu HF, Hui S, Chu RQ, Li GR, et al. 2005. Local elasticity imaging of ferroelectric domains in $\text{Pb}(\text{Mg}_{1/3}\text{Nb}_{2/3})\text{O}_3$ - PbTiO_3 single crystals by low-frequency atomic force acoustic microscopy. *Solid State Commun.* 133:521-25
68. Crozier KB, Yaralioglu GG, Degertekin FL, Adams JD, Minne SC, Quate CF. 2000. Thin film characterization by atomic force microscopy at ultrasonic frequencies. *Appl. Phys. Lett.* 76:1950-52
69. Sulchek T, Hsieh R, Adams JD, Yaralioglu GG, Minne SC, et al. 2000. High-speed tapping mode imaging with active Q control for atomic force microscopy. *Appl. Phys. Lett.* 76:1473-75
70. Amelio S, Goldade AV, Rabe U, Scherer V, Bhushan B, Arnold W. 2001. Measurements of elastic properties of ultra-thin diamond-like carbon coatings using atomic force acoustic microscopy. *Thin Solid Films* 392:75-84
71. Kopycinska-Muller M, Geiss RH, Muller J, Hurley DC. 2005. Elastic-property measurements of ultrathin films using atomic force acoustic microscopy. *Nanotechnology* 16:703-9
72. Hurley DC, Turner JA. 2004. Humidity effects on the determination of elastic properties by atomic force acoustic microscopy. *J. Appl. Phys.* 95:2403-7
73. Passeri D, Bettucci A, Germano M, Rossi M, Alippi A, et al. 2005. Effect of tip geometry on local indentation modulus measurement via atomic force acoustic microscopy technique. *Rev. Sci. Instrum.* 76:093904
74. Batog GS, Baturin AS, Bormashov VS, Sheshin EP. 2006. Calculation of the thicknesses and elastic properties of thin-film coatings using atomic-force acoustic microscopy data. *Tech. Phys.* 51:1084-89
75. Kopycinska-Muller M, Geiss RH, Hurley DC. 2006. Contact mechanics and tip shape in AFM-based nanomechanical measurements. *Ultramicroscopy* 106:466-74
76. Burnham N, Kulik A, Gremaud G, Gallo P, Oulevey F. 1996. Scanning local-acceleration microscopy. *J. Vac. Sci. Technol. B* 14:794-99
77. Cretin B, Vairac P. 1997. Optical detection for scanning microdeformation microscopy. *Appl. Phys. Lett.* 71:2082-84
78. Hesjedal T, Chilla E, Frohlich HJ. 1997. Scanning acoustic tunneling microscopy and spectroscopy: a probing tool for acoustic surface oscillations. *J. Vac. Sci. Technol. B* 15:1569-72
79. Jersch J, Demming F, Fedotov I, Dickmann K. 1999. Direct scanning tunneling microscope detection of laser induced ultrasonic pulses with nanometer resolution. *Rev. Sci. Instrum.* 70:4579-81
80. Cuberes MT, Assender HE, Briggs GAD, Kolosov OV. 2000. Heterodyne force microscopy of PMMA/rubber nanocomposites: nanomapping of viscoelastic response at ultrasonic frequencies. *J. Phys. D* 33:2347-55
81. Inagaki K, Kolosov OV, Briggs GAD, Wright OB. 2000. Waveguide ultrasonic force microscopy at 60 MHz. *Appl. Phys. Lett.* 76:1836-38
82. Nath R, Carcia RE, Blenell JE, Huey BD. 2007. The influence of grain boundaries and texture on ferroelectric domain hysteresis. *JOM* January:17-21
83. Shekhawat GS, Dravid VP. 2005. Nanoscale imaging of buried structures via scanning near-field ultrasound holography. *Science* 310:89-92

84. Szoszkiewicz R, Kulik AJ, Gremaud G, Lekka M. 2005. Probing local water contents of in vitro protein films by ultrasonic force microscopy. *Appl. Phys. Lett.* 86:123901
85. Manalis SR, Minne SC, Quate CF. 1996. Atomic force microscopy for high speed imaging using cantilevers with an integrated actuator and sensor. *Appl. Phys. Lett.* 68:871-73
86. Su Y, Brunnschweiler A, Evans AGR, Ensell G. 1999. Piezoresistive silicon V-AFM cantilevers for high-speed imaging. *Sensors Actuators A* 76:139-44
87. Hosaka S, Etoh K, Kikukawa A, Koyanagi H. 2000. Megahertz silicon atomic force microscopy (AFM) cantilever and high-speed readout in AFM-based recording. *J. Vac. Sci. Technol. B* 18:94-99
88. Lee DW, Ono T, Esashi M. 2000. High-speed imaging by electro-magnetically actuated probe with dual spring. *J. Microelectromech. Sys.* 9:419-24
89. Vettiger P, Despont M, Drechsler U, Durig U, Haberle W, et al. 2000. The "millipede": more than one thousand tips for future AFM data storage. *IBM J. Res. Dev.* 44:323-40
90. Ando T, Kodera N, Takai E, Maruyama D, Saito K, Toda A. 2001. A high-speed atomic force microscope for studying biological macromolecules. *Proc. Natl. Acad. Sci. USA* 98:12468-72
91. Degertekin FL, Hadimioglu B, Sulchek T, Quate CF. 2001. Actuation and characterization of atomic force microscope cantilevers in fluids by acoustic radiation pressure. *Appl. Phys. Lett.* 78:1628-30
92. Kawakatsu H, Kawai S, Saya D, Nagashio M, Kobayashi D, et al. 2002. Towards atomic force microscopy up to 100 MHz. *Rev. Sci. Instrum.* 73:2317-20
93. Kim YS, Nam HJ, Cho SM, Hong JW, Kim DC, Bu JU. 2003. PZT cantilever array integrated with piezoresistor sensor for high speed parallel operation of AFM. *Sensors Actuators A* 103:122-29
94. Houlet LF, Yamaguchi H, Miyashita S, Hirayama Y. 2004. InAs/AlGaSb piezoresistive cantilever for sub-angstrom scale displacement detection. *Jpn. J. Appl. Phys. Pt. 2* 43:L424-26
95. Bargatin I, Myers EB, Arlett J, Gudlewski B, Roukes ML. 2005. Sensitive detection of nanomechanical motion using piezoresistive signal downmixing. *Appl. Phys. Lett.* 86:133109
96. Fujimoto I, Suhara W, Kobayashi M, Goto T, Miyashita H, et al. 2005. High speed AFM image of inositol 1,4,5-trisphosphate receptor (IP3R) tetramer structure. *J. Neurochem.* 94:260
97. Kodera N, Yamashita H, Ando T. 2005. Active damping of the scanner for high-speed atomic force microscopy. *Rev. Sci. Instrum.* 76:053708
98. Hansma PK, Schitter G, Fantner GE, Prater C. 2006. Applied physics: high-speed atomic force microscopy. *Science* 314:601-2
99. Hobbs JK, Vasilev C, Humphris ADL. 2005. Real time observation of crystallization in polyethylene oxide with video rate atomic force microscopy. *Polymer* 46:10226-36
100. Humphris ADL, Miles MJ, Hobbs JK. 2005. A mechanical microscope: high-speed atomic force microscopy. *Appl. Phys. Lett.* 86:034106



Contents

MATERIALS CHARACTERIZATION

Low-Temperature Degradation of Zirconia and Implications for Biomedical Implants <i>Jérôme Chevalier, Laurent Gremillard, and Sylvain Deville</i>	1
Single-Molecule Micromanipulation Techniques <i>K. C. Neuman, T. Lionnet, and J.-F. Allemand</i>	33
Spin-Polarized Scanning Tunneling Microscopy of Magnetic Structures and Antiferromagnetic Thin Films <i>Wulf Wulfbekel and Jürgen Kirschner</i>	69
Microscale Characterization of Mechanical Properties <i>K. J. Hemker and W. N. Sharpe, Jr.</i>	93
Three-Dimensional Atom-Probe Tomography: Advances and Applications <i>David N. Seidman</i>	127
The Study of Nanovolumes of Amorphous Materials Using Electron Scattering <i>David J. H. Cockayne</i>	159
Nanoscale Electromechanics of Ferroelectric and Biological Systems: A New Dimension in Scanning Probe Microscopy <i>Sergei V. Kalinin, Brian J. Rodriguez, Stephen Jesse, Edgar Karapetian, Boris Mirman, Eugene A. Eliseev, and Anna N. Morozovska</i>	189
AFM and Acoustics: Fast, Quantitative Nanomechanical Mapping <i>Bryan D. Huey</i>	351
Electron Holography: Applications to Materials Questions <i>Hannes Lichte, Petr Formanek, Andreas Lenk, Martin Linck, Christopher Matzcek, Michael Lehmann, and Paul Simon</i>	539
Three-Dimensional Characterization of Microstructure by Electron Back-Scatter Diffraction <i>Anthony D. Rollett, S.-B. Lee, R. Campman, and G.S. Rohrer</i>	627

Atom Probe Tomography of Electronic Materials <i>Thomas F. Kelly, David J. Larson, Keith Thompson, Roger L. Alvis, Joseph H. Bunton, Jesse D. Olson, and Brian P. Gorman</i>	681
Electron Holography: Phase Imaging with Nanometer Resolution <i>Martha R. McCartney and David J. Smith</i>	729
FERROELECTRICS AND RELATED MATERIALS, David R. Clarke and Venkatraman Gopalan, Guest Editors	
Atomic-Level Simulation of Ferroelectricity in Oxides: Current Status and Opportunities <i>Simon R. Phillpot, Susan B. Sinnott, and Aravind Asthagiri</i>	239
Ferroelectric Domain Breakdown <i>Michel Molotskii, Yossi Rosenwaks, and Gil Rosenman</i>	271
Local Structure of Ferroelectric Materials <i>T. Egami</i>	297
Terahertz Polaritonics <i>T. Feurer, Nikolay S. Stoyanov, David W. Ward, Joshua C. Vaughan, Eric R. Statz, and Keith A. Nelson</i>	317
Spiral Magnets as Magnetoelectrics <i>T. Kimura</i>	387
Universal Domain Wall Dynamics in Disordered Ferroic Materials <i>W. Kleemann</i>	415
Defect–Domain Wall Interactions in Trigonal Ferroelectrics <i>Venkatraman Gopalan, Völkmar Dierolf, and David A. Scrymgeour</i>	449
Influence of Electric Field and Mechanical Stresses on the Fracture of Ferroelectrics <i>Gerold A. Schneider</i>	491
Strain Tuning of Ferroelectric Thin Films <i>Darrell G. Schlom, Long-Qing Chen, Chang-Beom Eom, Karin M. Rabe, Stephen K. Streiffer, and Jean-Marc Triscone</i>	589
Ferroelectric Epitaxial Thin Films for Integrated Optics <i>Bruce W. Wessels</i>	659

Index

Cumulative Index of Contributing Authors, Volumes 33–37	769
---	-----

Errata

An online log of corrections to *Annual Review of Materials Research* chapters (if any, 1997 to the present) may be found at <http://matsci.annualreviews.org/errata.shtml>